

See discussions, stats, and author profiles for this publication at: <https://www.researchgate.net/publication/262301150>

Lithium Migration in $\text{Li}_4\text{Ti}_5\text{O}_{12}$ Studied Using in Situ Neutron Powder Diffraction

ARTICLE in CHEMISTRY OF MATERIALS · APRIL 2014

Impact Factor: 8.35 · DOI: 10.1021/cm5002779

CITATIONS

17

READS

92

5 AUTHORS, INCLUDING:



Wei Kong Pang

Australian Nuclear Science and Technology Or...

65 PUBLICATIONS 253 CITATIONS

SEE PROFILE



Neeraj Sharma

Australian Nuclear Science and Technology Or...

52 PUBLICATIONS 557 CITATIONS

SEE PROFILE



She-huang Wu

Tatung University

37 PUBLICATIONS 703 CITATIONS

SEE PROFILE

Lithium Migration in $\text{Li}_4\text{Ti}_5\text{O}_{12}$ Studied Using in Situ Neutron Powder Diffraction

Wei Kong Pang,^{†,‡} Vanessa K. Peterson,^{*,†} Neeraj Sharma,[§] Je-Jang Shiu,^{||} and She-huang Wu^{*,||}

[†]Australian Nuclear Science and Technology Organization, Locked Bag 2001, Kirrawee DC, New South Wales 2232, Australia

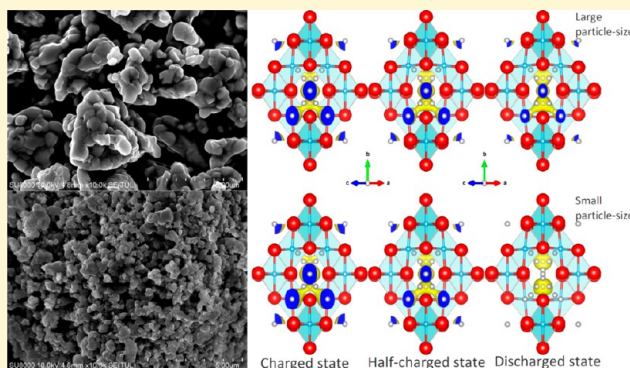
[‡]School of Mechanical, Materials, and Mechatronic Engineering, Institute for Superconducting & Electronic Materials, Faculty of Engineering, University of Wollongong, Wollongong, New South Wales 2522, Australia

[§]School of Chemistry, University of New South Wales, Sydney, New South Wales 2052, Australia

^{||}Department of Materials Engineering, Tatung University, No. 40, Sec. 3, Zhongshan North Road, Taipei City 104, Taiwan ROC

S Supporting Information

ABSTRACT: We used in situ neutron powder diffraction (NPD) to study the migration of Li in $\text{Li}_4\text{Ti}_5\text{O}_{12}$ anodes with different particle sizes during battery cycling. The motivation of this work was to uncover the mechanism of the increased capacity of the battery made with a smaller-particle-sized anode. In real time, we monitored the anode lattice parameter, Li distribution, and oxidation state of the Ti atom, and these suggested an increase in the rate of Li incorporation into the anode rather than a change in the migration pathway as a result of the particle size reduction. The lattice of these anodes during continuous lithiation undergoes expansion followed by a gradual contraction and then expansion again. The measured lattice parameter changes were reconciled with Li occupation at specific sites within the $\text{Li}_4\text{Ti}_5\text{O}_{12}$ crystal structure, where Li migrates from the 8a to 16c sites. Despite these similar Li-diffusion pathways, in larger-particle-sized $\text{Li}_4\text{Ti}_5\text{O}_{12}$ the population of Li at the 16c site is accompanied by Li depopulation from the 8a site, which is in contrast to the smaller-particle-sized anode where our results suggest that Li at the 8a site is replenished faster than the rate of transfer of Li to the 16c site. Fourier-difference nuclear density maps of both anodes suggest that 32e sites are involved in the diffusion pathway of Li. NPD is again shown to be an excellent tool for the study of electrode materials for Li-ion batteries, particularly when it is used to probe real-time crystallographic changes of the materials in an operating battery during charge–discharge cycling.

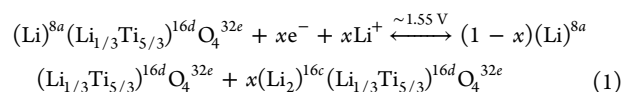


INTRODUCTION

Since Sony Corporation introduced the first commercial Li-ion battery (LIB) in 1991, featuring LiCoO_2 and graphite as the cathode and anode, respectively, LIBs have now become extensively used for energy storage because of their relatively high energy density, long cycle life, and low cost.¹ However, the increasing demands placed on LIBs, including better electrochemical performance and safer operation, mandate further development of battery materials.

Spinel $\text{Li}_4\text{Ti}_5\text{O}_{12}$ is a well-known zero-strain insertion compound that is an alternative anode to the widely used carbonaceous materials. This is because $\text{Li}_4\text{Ti}_5\text{O}_{12}$ shows an exceptionally high rate performance, excellent cycling stability, and good Li-insertion electrochemistry with a formal potential of ~ 1.55 V versus Li^+/Li as an anode in LIBs.^{2–6} As a result of the high redox potential of $\text{Li}_4\text{Ti}_5\text{O}_{12}$, the formation of a solid electrolyte interface layer^{7–10} and Li-metal deposition¹¹ on the surface of the anode, which are all detrimental to LIB use, can be prevented. It is generally accepted that the Li (de)-intercalation reaction in $\text{Li}_4\text{Ti}_5\text{O}_{12}$ proceeds through a

reversible two-phase reaction (eq 1), resulting in flat plateaus of the charge and discharge curves.



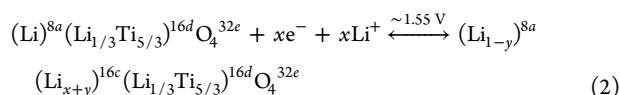
where the superscripts are the crystallographic sites. $(\text{Li})^{8a}(\text{Li}_{1/3}\text{Ti}_{5/3})^{16d}\text{O}_4^{32e}$ and $(\text{Li}_2)^{16c}(\text{Li}_{1/3}\text{Ti}_{5/3})^{16d}\text{O}_4^{32e}$ crystallize in the $Fd\bar{3}m$ space group with similar lattice parameters and are referred to as $\text{Li}_4\text{Ti}_5\text{O}_{12}$ and $\text{Li}_7\text{Ti}_5\text{O}_{12}$, respectively. The difference in the lattice parameters between $\text{Li}_4\text{Ti}_5\text{O}_{12}$ and $\text{Li}_7\text{Ti}_5\text{O}_{12}$ is less than 0.1%, with the latter lattice being slightly smaller.^{3,4} In both phases, $1/6$ of 16d sites are occupied by electrochemically inert Li^+ , with the remainder being Ti^{4+} . The electrochemically active Li^+ occupies tetrahedral (8a) sites in $\text{Li}_4\text{Ti}_5\text{O}_{12}$. During charge (Li insertion) and to minimize strain, the electrochemically active Li^+ is relocated to the octahedral

Received: January 23, 2014

Revised: March 12, 2014

Published: March 14, 2014

(16c) sites together with the newly inserted Li^+ , forming $\text{Li}_7\text{Ti}_5\text{O}_{12}$. In contrast to this more popular theory,^{2–8} Wagemaker et al. report that the two-phase system is found only at temperatures below 100 K and that single-phase $\text{Li}_4\text{Ti}_5\text{O}_{12}$ is found at room temperature, where a gradual change in the $\text{Li}_4\text{Ti}_5\text{O}_{12}$ lattice parameter occurs during charging in a process in which mixed 8a/16c occupation by Li exists.¹² The high rate capability of $\text{Li}_{4+z}\text{Ti}_5\text{O}_{12}$ ($z = 0–3$) is attributed to solid-solution-induced disorder involving the mixed 8a/16c occupation.¹² Wagemaker et al. report the Li (de)intercalation of $\text{Li}_4\text{Ti}_5\text{O}_{12}$ to occur via the following solid-solution reaction (eq 2)



where $x = z/3$ and $y \leq 1$.

The phase transition between $\text{Li}_4\text{Ti}_5\text{O}_{12}$ and $\text{Li}_{4+z}\text{Ti}_5\text{O}_{12}$ (or $\text{Li}_7\text{Ti}_5\text{O}_{12}$ in the two-phase mechanism) involves a relatively small change in the lattice parameters and similar crystal structures. Notably, the underlying mechanism of the phase transition remains controversial and, importantly, may control the performance of the $\text{Li}_4\text{Ti}_5\text{O}_{12}$ anodes. For example, it is known that electrodes prepared by different methods with correspondingly different particle sizes can have different electrochemical performance, which is led by a distribution of redox potentials in the near-surface area, increased contact area with the electrolyte, and shorter Li-diffusion distance.^{13–18} Thus, characterizing the Li^+ -insertion/extraction mechanisms of samples with different particle sizes will yield insight into how battery performance may be improved by modifying the $\text{Li}_4\text{Ti}_5\text{O}_{12}/\text{Li}_7\text{Ti}_5\text{O}_{12}$ anode.

Increasingly, neutron powder diffraction (NPD) has been used to study LIBs. Cai et al.¹⁹ used in situ NPD to study the inhomogeneous degradation of electrodes in large-format LIBs, and whilst we^{20–25} used in situ NPD to study the non-equilibrium phase transitions of electrodes in LIBs. In particular, the relatively large penetration depth and non-destructive interaction of neutrons with matter allows NPD to probe the bulk crystallography of electrodes in functioning batteries in real time. The sensitivity of NPD to light elements such as Li and O in the presence of heavier ones can also enable the direct measurement of the Li content and its location within electrodes while at the same time allowing for the determination of redox-active couples by tracking the transition-metal valence via the oxygen to transition-metal distance. With these advantages, NPD can be useful in studying near zero-strain materials such as $\text{Li}_4\text{Ti}_5\text{O}_{12}$ during battery function. Colin et al.²⁶ tracked the Li occupation during its migration from the 8a to the 16c site in $\text{Li}_7\text{Ti}_5\text{O}_{12}$ by examining the evolution of the $\text{Li}_7\text{Ti}_5\text{O}_{12}$ 773 and 666 reflection intensities with battery charge using NPD. More recently, our work²¹ correlated the Ti oxidation state to the intensity of the $\text{Li}_4\text{Ti}_5\text{O}_{12}$ 222 reflection by studying the change in the O positional parameter during charge/discharge cycling in a $\text{LiNi}_{0.5}\text{Mn}_{1.5}\text{O}_4/\text{Li}_4\text{Ti}_5\text{O}_{12}$ full cell.

In this work, we used in situ NPD to determine the phase evolution of two $\text{Li}_4\text{Ti}_5\text{O}_{12}$ anode materials prepared by different methods; we determined that the materials have different particle sizes and electrochemical performance but the same phase composition and crystallography. $\text{Li}_4\text{Ti}_5\text{O}_{12}$ is the limiting electrode in the neutron-friendly battery, which was assembled using deuterated electrolyte and the relatively well-

studied olivine LiFePO_4 cathode, with the latter having many merits as an advanced cathode material that has been used commercially for large-format LIBs since its introduction by Padhi et al. in 1997.^{27,28} We examined the lithiation/delithiation mechanism of $\text{Li}_4\text{Ti}_5\text{O}_{12}$ alongside the typical two-phase transition of LiFePO_4 by galvanostatically charging and discharging the battery within the 1.0–3.0 V window (vs $\text{Li}_4\text{Ti}_5\text{O}_{12}$). We also investigated the formation of $\text{Li}_{4+z}\text{Ti}_5\text{O}_{12}$ by applying a 5 h potentiostatic regime at 3.0 V. The diffusion path of Li within the anode during charge and discharge is proposed on the basis of the analysis of the in situ NPD data. The dissimilarities between the functionality of two $\text{Li}_4\text{Ti}_5\text{O}_{12}$ anodes were uncovered and are discussed.

■ EXPERIMENTAL SECTION

LiFePO_4 cathode powders were provided by Tatung Fine Chemicals Co., Taiwan. $\text{Li}_4\text{Ti}_5\text{O}_{12}$ anode powders were prepared with different particle sizes. Larger-particle-sized $\text{Li}_4\text{Ti}_5\text{O}_{12}$ (LTO-1) was prepared by a sol–gel method using lithium nitrate (100%, Wako) and titanium butoxide (98.0%, Acros). The stoichiometrically mixed powders (Li/Ti = 4:5) were added to a solution of citric acid (CA) (99.5%, Acros) and ethylene glycol (EG) (99.5%, Acros) (CA/EG = 1:4) at 85 °C for 5 h to become sols. The sols were heated at 100 and 180 °C to remove water and excess EG, respectively, and to form gels. The gels were then calcined at 350 °C for 4 h followed by heat treatment at 850 °C for 10 h. $\text{Li}_4\text{Ti}_5\text{O}_{12}$ powders with a smaller particle size (LTO-2) were also prepared via a sol–gel method but using lithium acetate (98%, Acros) instead of lithium nitrate. The stoichiometrically mixed powders were dissolved in an adequate amount of ethanol (99.5%, Shimadzu), and the solution was aged for 3 h to form a white-colored gel. The resulting gel was heated at 80 °C to yield an organic precursor with a fine white product powder obtained by heat treating in air at 800 °C for 4 h.

High-resolution NPD data were collected using ECHIDNA, the high-resolution neutron powder diffractometer at the Open Pool Australian Lightwater (OPAL) research reactor at the Australian Nuclear Science and Technology Organization (ANSTO).²⁹ The neutron beam wavelength was 1.6214(4) Å, which was determined using the La^{11}B_6 NIST standard reference material 660b. The NPD data were obtained in the 2θ angular range 4 to 164° with a step size of 0.125°. Rietica ver. 1.77³⁰ was employed to perform Rietveld analysis of the high-resolution NPD data. The refineable parameters include the background coefficients, zero-shift and peak-shape parameters, lattice parameters, O positional parameters, and isotropic atomic displacement parameters.

The morphology of the as-prepared samples was investigated using field-emission scanning electron microscopy with a SU8000 (Hitachi, Japan) instrument. All observations were carried out without a conductive coating and with a 10 kV acceleration voltage. The particle-size distribution of the as-prepared samples was examined using a LS 13 320 (Beckman Coulter, Canada) particle-size analyzer.

Specially designed pouch-type batteries were used in the collection of the in situ NPD data from the LTO-1 and LTO-2 anodes. The LiFePO_4 cathode was prepared by casting a slurry of the active materials (80 wt %), acetylene black (10 wt %), and poly(vinylidene difluoride) (PVDF) binder (10 wt %) onto Al foil. The loading ratio between the anode and cathode was designed to be ~4:6 by weight. The electrodes were cut into $1 \times 4 \text{ cm}^2$ strips. Immobilon-P PVDF membrane (Millipore) was used as a separator because of its lower H content relative to the conventionally used Celgard membrane, where the strong incoherent neutron scattering of H is detrimental to the NPD signal. The $\text{LiFePO}_4/\text{Li}_4\text{Ti}_5\text{O}_{12}$ batteries were prepared by stacking 30 anode/separator/cathode assemblies with a parallel connection. The stack was placed in an Ar-filled glovebox for 24 h and then wrapped in a polypropylene-coated Al foil to form a pouch. The dimensions of the prepared cell were 1.5 cm in width (including the sealing junction of the Al pouch), 10 cm in length (including electrode handles), and 1 cm in thickness. Prior to the in situ NPD

experiment, deuterated electrolyte solution (1 M lithium hexafluorophosphate (99.99%, Sigma-Aldrich) in a 1:1 volume ratio of deuterated dimethyl carbonate (99.5%, Novachem) to deuterated ethylene carbonate (98%, Novachem)) was injected into the pouch, which was heat-sealed under Ar. After 1 day of wetting, the batteries were used in the in situ NPD experiment. The batteries containing LTO-1 and LTO-2 anodes are termed battery-1 and battery-2, respectively. During the in situ NPD experiment, both batteries were cycled galvanostatically using a potentiostat/galvanostat (Autolab PG302N) at currents of 11 mA (theoretically equivalent to 0.1 C) for two cycles between 1.0 and 3.0 V (vs $\text{Li}_4\text{Ti}_5\text{O}_{12}$). In the second cycle, a constant voltage step at 3.0 V for 5 h was applied.

In situ NPD data of the $\text{LiFePO}_4/\text{Li}_{4+z}\text{Ti}_5\text{O}_{12}$ batteries were collected using WOMBAT,³¹ the high-intensity neutron powder diffractometer at the OPAL research reactor at ANSTO. WOMBAT features an area detector that continuously covers 120° in 2θ and has a relatively intense neutron beam, allowing the rapid collection of data. A neutron beam with a wavelength of $2.9592(2)$ Å was used, which was determined using the La^{11}B_6 NIST standard reference material 660b. The diffractograms were obtained with an exposure time of 5 min per pattern in the angular range $16.1\text{--}136.9^\circ$ in 2θ during charge–discharge cycling of the batteries. Sequential Rietveld refinements were carried out using the NPD data using FullProf with visualization in WinplotR.^{32,33} The refinements were performed using data in the range $60\text{--}120^\circ$ in 2θ . Single-peak fitting of the LiFePO_4 211 and 311 reflections, the FePO_4 222 reflection, and the $\text{Li}_{4+z}\text{Ti}_5\text{O}_{12}$ 004 reflection was performed using the Large Array Manipulation Program (LAMP).³⁴

RESULTS AND DISCUSSION

Using high-resolution NPD data, the crystallographic details of LiFePO_4 , LTO-1, and LTO-2 were established. LiFePO_4 was found to adopt the orthorhombic $Pnma$ ³⁵ space group symmetry, with the refined-fit profile shown in Figure S1 and crystallographic details obtained from Rietveld analysis in Table S1. Both LTO-1 and LTO-2 adopt $Fd\bar{3}m$ space group symmetry. In addition to the main $Fd\bar{3}m$ phase, a minor amount of monoclinic Li_2TiO_3 was also detected, 4.8(6) and 1.9(3) wt % in LTO-1 and LTO-2, respectively. The Rietveld refinement profiles for LTO-1 and LTO-2 are shown in Figure 1, panels a and b, respectively. The crystallographic details are summarized in Table S1 and indicate similar crystallographic features between LTO-1 and LTO-2.

The particle size and morphology of the as-prepared electrode materials are shown in the SEM micrographs in Figure 2. The LiFePO_4 particles are bar-like and are ~ 1 μm wide and ~ 3.5 μm long. Both LTO-1 and LTO-2 are cube-like and differ significantly in their average particle sizes, with SEM showing LTO-1 to have an average primary particle size of ~ 500 nm and LTO-2, ~ 200 nm. Particle-size distributions are shown in the inset of Figure 2, where the mean particle sizes, similar to the SEM analysis, show LTO-1 particles to be approximately twice as large as LTO-2 particles. The larger particle size determined in the particle-size distribution analysis relative to that obtained using SEM likely arises because of the measurement of agglomerates (the secondary particle size).

The collected NPD patterns of battery-1 and battery-2 during cycling are shown in Figure S3. Single-peak-fitting routines applied to the LiFePO_4 211 and 311 reflections and the FePO_4 221 reflection in the in situ NPD data are plotted in Figure S4. The results show that for both batteries the LiFePO_4 reflection positions remain nearly unchanged during the battery charge and discharge but that the LiFePO_4 reflection intensities decrease with increasing FePO_4 221 reflection intensity during battery charge. On discharge, the LiFePO_4 reflection intensities

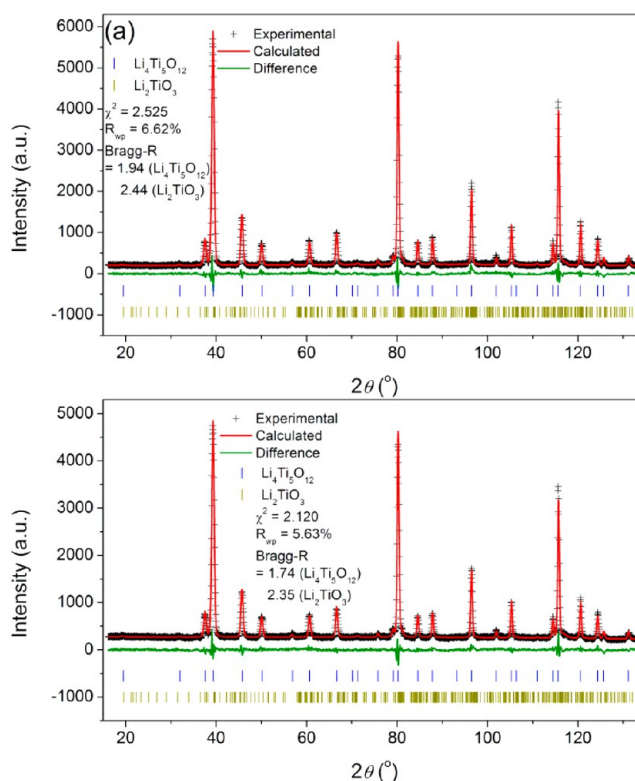


Figure 1. Rietveld profile fits for (a) LTO-1 and (b) LTO-2 using high-resolution NPD data. Measured data are shown as crosses, and the calculation is the solid line through the measured data. The difference between the measured and calculated patterns is shown along the bottom of the plots. The figures of merit include the Bragg statistical reliability factor (Bragg-R), the profile factor (R_p), the weighted profile factor (R_{wp}), and the goodness-of-fit (χ^2) term. Vertical bars represent the reflection positions for each of the phases. The profile fit for LiFePO_4 is shown in Figure S1.

increase with decreasing FePO_4 reflection intensities, suggesting that a two-phase reaction occurs during lithiation and delithiation of the LiFePO_4 cathode, in agreement with previous work.^{27,28}

We model the lattice evolution of the $\text{Li}_{4+z}\text{Ti}_5\text{O}_{12}$ anode as a single phase (solid-solution reaction) after Wagemaker et al.,¹² the details of which are presented in Table S2. The Rietveld-refined fit profiles of battery-1 and battery-2 are shown in Figure S5a and b, and the ranges of the figures of merit, including χ^2 , R_{wp} , and Bragg-R factors, are summarized in Table S3.

We first considered the phase fraction of the active materials inside the batteries. Before cycling, Rietveld analysis shows that the two batteries have a similar anode to cathode weight ratio (45:55), in agreement with their construction. During charging, the phase fraction of LiFePO_4 decreases monotonically with the increasing fraction of FePO_4 as a result of the two-phase reaction found from the single-peak fitting. The phase fraction of $\text{Li}_{4+z}\text{Ti}_5\text{O}_{12}$ remains relatively stable (Figure 3), as expected from the solid-solution model. In comparison, a relatively higher phase fraction of FePO_4 was found in battery-2 relative to battery-1, and this is correlated to the higher capacity of battery-2. At the same anode to cathode weight ratio and same applied current, we found that LTO-2 exhibits a better rate capability than LTO-1, as expected from the smaller-particle-sized LTO-2.

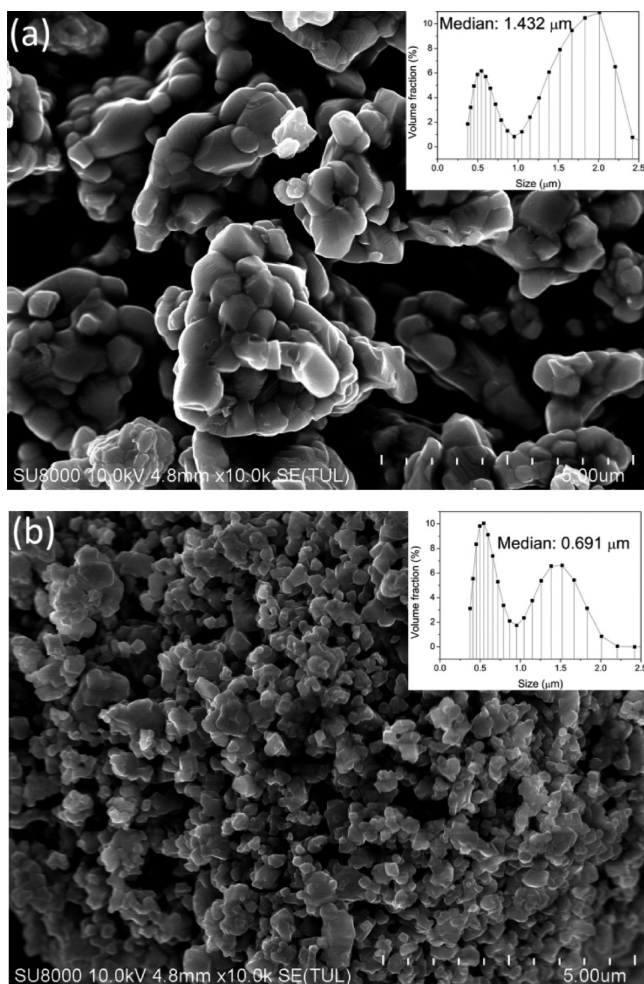


Figure 2. SEM micrographs of the as-prepared (a) LTO-1 and (b) LTO-2 powders. Particle-size distributions are shown in the insets.

Besides the variation in the phase composition, the details of the $\text{Li}_{4+z}\text{Ti}_5\text{O}_{12}$ lattice during charge and discharge were also extracted. Interestingly, the NPD data revealed that the $\text{Li}_{4+z}\text{Ti}_5\text{O}_{12}$ lattice is perturbed from a simple contraction during charging (Li insertion) and expansion during discharging (Li extraction) (Figure 4). Single-peak fitting results support this unexpected observation. Notably, this work has uncovered that during continuous lithiation both anodes undergo the following process: lattice expansion followed by gradual contraction followed by further expansion.

During the first cycle of LTO-1, the lattice parameter increases to 8.3619(5) Å after 135 min of charging (a 0.03(1)% increase) followed by a decrease to 8.3584(6) Å at 420 min (a 0.04(1)% decrease) followed again by a sudden increase to 8.3600(6) Å (a 0.02(1)% increase) at the end of the first charge (3.0 V vs $\text{Li}_4\text{Ti}_5\text{O}_{12}$). On discharge, the lattice parameter drops to 8.3572(6) Å (a 0.03(1)% decrease) and then monotonically increases to 8.3613(6) Å (increasing by 0.05(1)%) at the end of the discharge. A sudden decrease in the lattice parameter at the beginning of delithiation was observed when the sign of the applied current changes. For LTO-2, the lattice parameter increases to 8.3649(5) Å after 110 min of charging (a 0.01(1)% increase) followed by a linear decrease to 8.3603(6) Å (a 0.05(1)% decrease) at 710 min (the end of charge at 3.0 V vs $\text{Li}_4\text{Ti}_5\text{O}_{12}$). On discharge, the LTO-2 lattice parameter linearly increases to 8.366(5) Å (by 0.07(1)%) at 1140 min (1.0 V vs

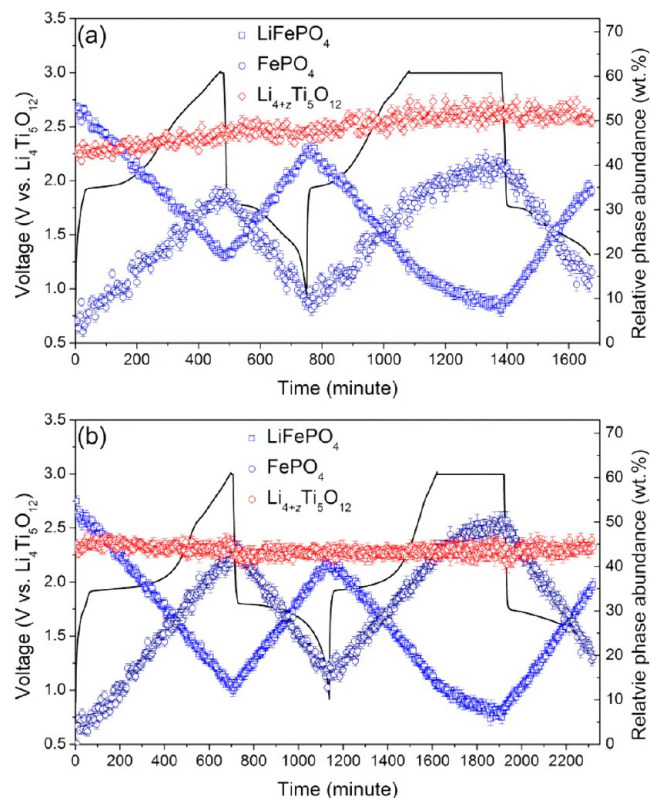


Figure 3. Relative phase abundance of the LiFePO_4 (blue), $\text{Li}_4\text{Ti}_5\text{O}_{12}$ (red), and delithiated FePO_4 (dark blue) phases upon the cycling of battery-1 (a) and battery-2 (b). The total amount of active phase (cathode and anode) is normalized to 100%. Battery voltage is also shown.

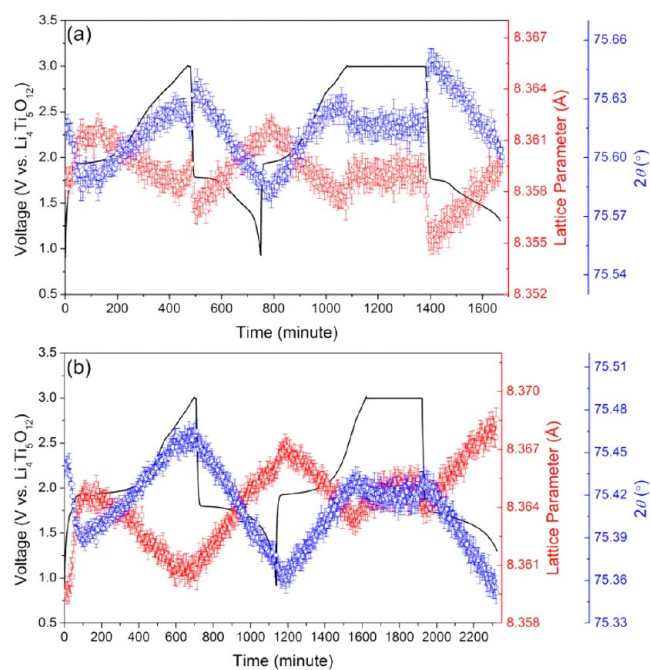


Figure 4. Variation of the LTO-1 (a) and LTO-2 (b) lattice parameter (red) and 222 reflection intensity (blue) during charge–discharge cycling. Battery voltage is also shown.

$\text{Li}_4\text{Ti}_5\text{O}_{12}$), but we note that the sudden decrease in the lattice parameter observed for LTO-1 at the beginning of delithiation

is not observed for LTO-2. The larger change in the lattice parameter and the higher capacity achieved for LTO-2 compared with LTO-1 suggest that more Li^+ are accommodated in the LTO-2 anode. Given that the particle size is proportional to the length of the mean free Li^+ -diffusion path,^{13–17} this likely enables more Li^+ to migrate in LTO-2 than in LTO-1 over the same time period.

During the second cycle, similar variations as those seen in the first cycle were observed in the LTO-1 and LTO-2 lattice with the exception of the 5 h potentiostatic step. At the start of the potentiostatic step (3.0 V vs $\text{Li}_4\text{Ti}_5\text{O}_{12}$), the current drops significantly and the gained capacity increases slowly (Figure S6). Consequently, the lattice parameter of both anodes changes very little. At the end of the potentiostatic step, both anodes exhibit a sudden increase in their lattice, although this feature is less pronounced for LTO-2. Given the higher capacity of LTO-2, it is possible that the LTO-1 lattice increase that occurs during the first charge process takes place in LTO-2 but occurs too quickly to be captured in the NPD data. We note that although the LTO-1 and LTO-2 lattice response during the same electrochemical charge and discharge are slightly different from each other, LTO-1 and LTO-2 are structurally similar. According to Vegard's law,^{36,37} the slightly different LTO-1 and LTO-2 lattice parameter evolution likely reflect differences in Li content during battery cycling. A consideration of the lattice evolution in terms of the state-of-charge (SOC) of the battery for the first charge shows that although the LTO-2 lattice changes faster than that of LTO-1, the lattice parameter variation follows similar trends. Both $\text{Li}_{4+z}\text{Ti}_5\text{O}_{12}$ lattices undergo expansion up to 15% SOC followed by a gradual contraction followed again by expansion (last 5% SOC) (Figure S7). Quantitatively, we note that during the gradual contraction observed from approximately 15–90% SOC the LTO-2 lattice changes 28.8(7)% more quickly than that of LTO-1. We note again that the different variation in the lattice parameters of LTO-1 and LTO-2 during charge/discharge reflects differences in Li distribution during lithiation and delithiation and that the lattice relaxation at the beginning of delithiation observed in LTO-1, but not in LTO-2, may arise as a result of this.

As a first approach to understanding the variation of Li in $\text{Li}_{4+z}\text{Ti}_5\text{O}_{12}$ during charge/discharge cycling, we examined the changes in intensity of particular $\text{Li}_{4+z}\text{Ti}_5\text{O}_{12}$ reflections. Figure 5 shows the intensity of the LTO-1 and LTO-2 222 and 004 reflections as a function of lithiation, where the 222 reflection intensity increases and the 004 reflection decreases during lithiation.

Given that the $\text{Li}_4\text{Ti}_5\text{O}_{12}$ (222) plane is filled by Ti and Li atoms at the 16d site, that both atoms have a negative coherent neutron-scattering length (−1.9 and −3.438 fm, respectively), and that the $\text{Li}_4\text{Ti}_5\text{O}_{12}$ (004) plane is filled with O atoms at the 32e site and has a positive coherent neutron-scattering length (5.803 fm) (Figure 6), the inserted and repositioned Li needs to occupy a site common to both planes to result in the observed intensity changes during lithiation (this being the 16c site). This observation is consistent with the reported $\text{Li}_4\text{Ti}_5\text{O}_{12}$ – $\text{Li}_7\text{Ti}_5\text{O}_{12}$ transition mechanism where the inserted Li occupies the 16c site upon forming $\text{Li}_{4+z}\text{Ti}_5\text{O}_{12}$ ($\text{Li}_7\text{Ti}_5\text{O}_{12}$).^{3,4,12,17} Although the general trend of the $\text{Li}_4\text{Ti}_5\text{O}_{12}$ 004 and 222 reflection intensity change during lithiation is common between LTO-1 and LTO-2, there is a slight discrepancy in when the maximum intensity occurs, with LTO-2 achieving apparent saturation earlier, indicating that the

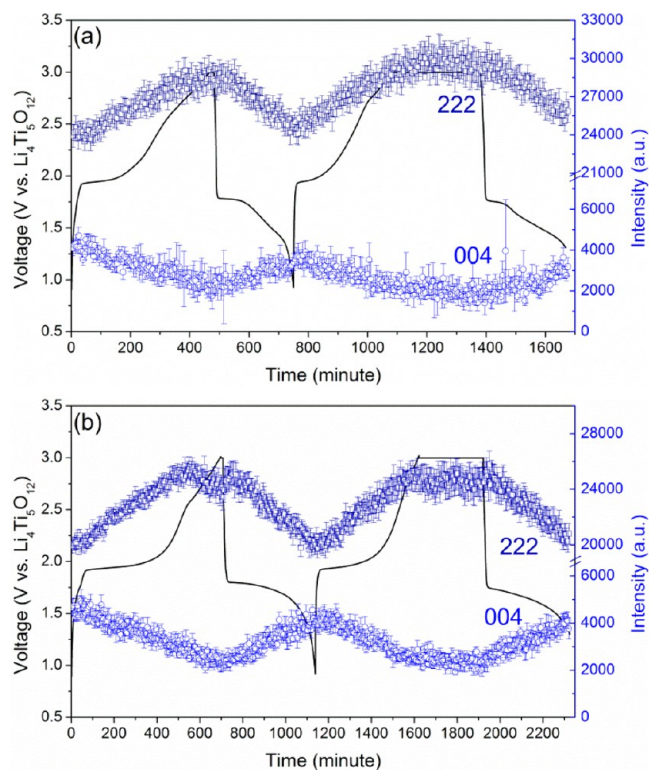


Figure 5. Variation of $\text{Li}_4\text{Ti}_5\text{O}_{12}$ 222 and 004 reflection intensities for LTO-1 (a) and LTO-2 (b) (shown in Table S1 during the first charge). Battery voltage is also shown.

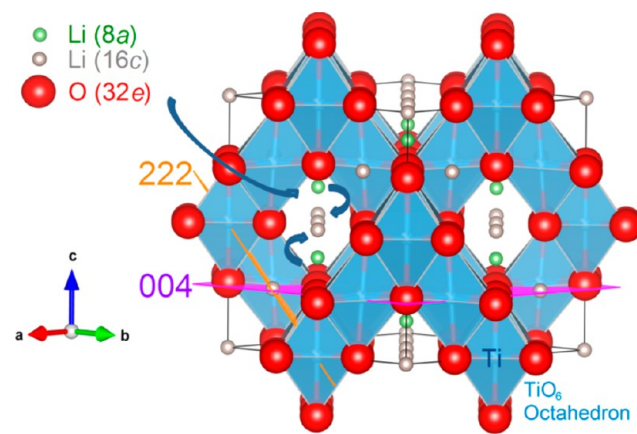


Figure 6. Crystal structure of $\text{Li}_{4+z}\text{Ti}_5\text{O}_{12}$ with the (222) and (004) planes indicated. The theoretical pathway of Li (inward) diffusion during lithiation is indicated by dark blue arrows. Ti is located at the center of the TiO_6 octahedra (16d site).

Li site occupation differs between the anodes, which is correlated to the greater capacity of battery-2.

Rietveld refinement of the $\text{Li}_{4+z}\text{Ti}_5\text{O}_{12}$ structure using the in situ NPD data revealed Li occupation at the 8a and 16c sites (Figure 6), consistent with that expected and also with the changes in reflection intensity discussed earlier. Extracting Li-site occupancy factors in $\text{Li}_4\text{Ti}_5\text{O}_{12}$ from the in situ NPD data is difficult, and to achieve this, it was necessary to constrain the structure by fixing the O positional parameter (to 0.265 = $x = y = z$), although in reality, the Li-site occupation is known to influence the O position. We refined the O positional parameter using the in situ NPD data in a separate analysis

to reveal the average valence of Ti, as will be discussed later. Nevertheless, the trends in Li-site occupancy factors at the 8a and 16c sites extracted from the Rietveld refinement are consistent with those expected during battery charge/discharge cycling (Figure 7).

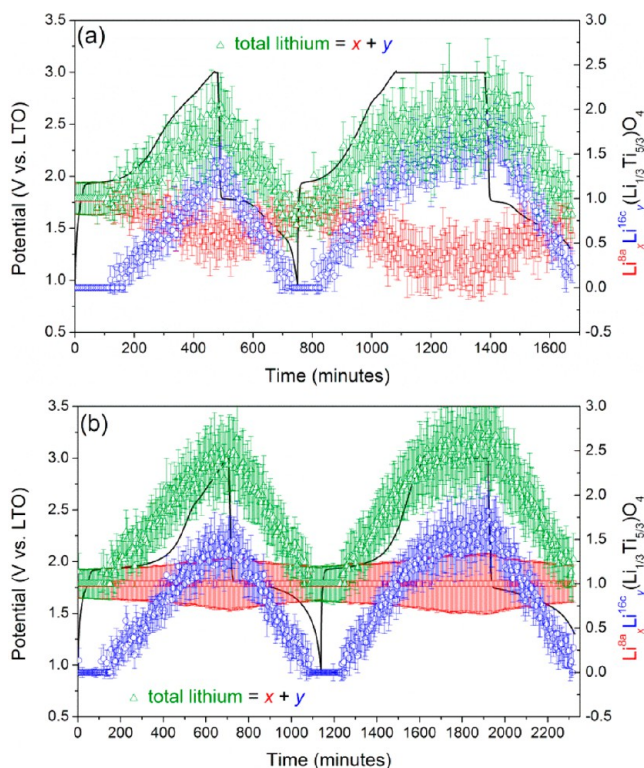


Figure 7. Li 8a and 16c site occupation and total Li content in LTO-1 (a) and LTO-2 (b) during charge–discharge cycling. Battery voltage is also shown.

At the end of the lithiation process, the site occupancy factors for Li at the 8a and 16c sites were 0.46(26) and 1.20(23) in LTO-1, respectively, forming $\text{Li}_{0.46(26)}^{8a}\text{Li}_{1.20(23)}^{16c}(\text{Li}_{1/3}\text{Ti}_{5/3})^{16d}\text{O}_{32e}^{4-}$. At the potentiostatic step (3.0 V vs $\text{Li}_4\text{Ti}_5\text{O}_{12}$) during the second charge, the current drops significantly and the gained capacity increases slowly with a slower lithiation rate compared to that of the galvanostatic charge, in agreement with the observed lattice parameter variation. The Li content in each $\text{Li}_{4+z}\text{Ti}_5\text{O}_{12}$ should be proportional to the battery capacity. Given that the amount of LTO-1 in the cell is approximately 680 mg and the charge capacity is 87.7 mA h (Figure S6), the final LTO-1 stoichiometry is expected to be $\text{Li}_{1.74}(\text{Li}_{1/3}\text{Ti}_{5/3})^{16d}\text{O}_{32e}^{4-}$. The Rietveld-derived site occupancy factors for Li (within calculation errors) are in agreement with this expected value, although we note that the Rietveld-derived content accounts only for Li that is ordered within the $\text{Li}_{4+z}\text{Ti}_5\text{O}_{12}$ structure. In

LTO-2, Li at the 16c site reaches a site occupancy factor of 1.47(30) at the end of lithiation, forming $\text{Li}_{1.47(30)}^{8a}\text{Li}_{1.47(30)}^{16c}(\text{Li}_{1/3}\text{Ti}_{5/3})^{16d}\text{O}_{32e}^{4-}$ ($\text{Li}_{7.41(\pm 1.3)}\text{Ti}_5\text{O}_{12}$). Although the deviation from the calculated charge capacity is relatively large, a composition of $\text{Li}_{7.25}\text{Ti}_5\text{O}_{12}$ is expected where the calculated and expected Li content are in agreement.

Differences between the time evolution of the Li-site occupancy factors in LTO-1 and LTO-2 are noted (Figure 7). The rate of lithiation (and delithiation) within $\text{Li}_{4+z}\text{Ti}_5\text{O}_{12}$ was determined by a linear fit to the time evolution of the Li content, including the site occupancy factors (Figures S8 and S9). Li intercalation and deintercalation rates for the first cycle of battery-1 are summarized in Table 1.

During initial lithiation, both $\text{Li}_{4+z}\text{Ti}_5\text{O}_{12}$ structures begin with Li fully occupied at the 8a site, which continues during lithiation until Li starts to populate the 16c site in both $\text{Li}_{4+z}\text{Ti}_5\text{O}_{12}$ structures, taking place at 110 min (1.95 V vs $\text{Li}_4\text{Ti}_5\text{O}_{12}$) for LTO-1 and essentially at the same time, 105 min (1.92 V vs $\text{Li}_4\text{Ti}_5\text{O}_{12}$), for LTO-2. The 16c sites populate (and depopulate during delithiation) at different rates in the two anodes. We found that Li at the 16c site populates at the rate of 0.0036(1) Li/min (0.216(6) $\text{Li}^+/\text{Li}_{4+z}\text{Ti}_5\text{O}_{12}/\text{h}$) in LTO-1 and at 0.0028(1) Li/min in LTO-2. The lower rate of Li population on charge (which we also found on depopulation during discharge) of the 16c site in LTO-2 compared to LTO-1 was unexpected given the higher capacity of LTO-2. This result, extracted from Rietveld analysis of the in situ NPD data, mimics the trend of the $\text{Li}_4\text{Ti}_5\text{O}_{12}$ 222 and 004 reflection intensities for LTO-1 and LTO-2 (the rates are shown in Table S4), indicating a slower rate of change of these in LTO-2 relative to LTO-1. In LTO-1 and during delithiation, Li occupation at the 8a site increases at the rate of 0.060(6) $\text{Li}^+/\text{LTO-1}/\text{h}$ 0.0010(1) $\text{Li}^+/\text{LTO-1}/\text{min}$, Figure S8a), but that at the 16c site decreases at the faster rate of 0.297(1) $\text{Li}^+/\text{LTO-1}/\text{h}$ until the end of the battery discharge.

Population of the 16c site with Li in LTO-1 is accompanied by a depletion of Li at the 8a site at the rate of 0.072(6) $\text{Li}^+/\text{Li}_{4+z}\text{Ti}_5\text{O}_{12}$ formula unit/h (0.0012(1) Li/min), indicating that Li is migrating from the 8a to the 16c site. Interestingly, in LTO-2, the Li-site occupancy factor at the 8a site remains saturated (full occupation), although we note that the estimated standard deviation associated with the Li 8a site occupancy factor in LTO-2 increases as lithiation proceeds (varying between 0.024 and 0.307). This result supports the theory that smaller particle sizes in $\text{Li}_{4+z}\text{Ti}_5\text{O}_{12}$ lead to larger capacities because simultaneous 8a and 16c occupation is more easily accommodated in the near-surface region of the particle compared to the bulk.¹⁸ There are two explanations for our observation of a static Li-site occupancy factor at the 8a site in LTO-2: first, the 8a site is being refilled from the electrolyte at a higher rate than the rate of transfer of Li to the 16c site and second, the 8a site does not participate in the electrochemical reaction. Our results indicate that the 8a site is being

Table 1. Li Intercalation and Deintercalation Rates in LTO-1 and LTO-2 during the First Cycle^a

	Li intercalation rate		Li deintercalation rate		total Li content (x + y)	
	$\text{Li}^+/\text{Li}_{4+z}\text{Ti}_5\text{O}_{12}/\text{min}$	$\text{Li}^+/\text{Li}_{4+z}\text{Ti}_5\text{O}_{12}/\text{h}$	$\text{Li}^+/\text{Li}_{4+z}\text{Ti}_5\text{O}_{12}/\text{min}$	$\text{Li}^+/\text{Li}_{4+z}\text{Ti}_5\text{O}_{12}/\text{h}$	expected	calculated
LTO-1	0.00234(2)	0.140(1)	0.00427(23)	0.256(14)	1.74	1.67(35)
LTO-2	0.00281(4)	0.169(2)	0.00450(3)	0.270(1)	2.09	2.47(43)

^aObtained from linear fits to the site occupancy factors or total $x + y$ in $\text{Li}_{1.47(30)}^{8a}\text{Li}_{1.47(30)}^{16c}(\text{Li}_{1/3}\text{Ti}_{5/3})^{16d}\text{O}_{32e}^{4-}$ as a function of time (Figures S8 and S9).

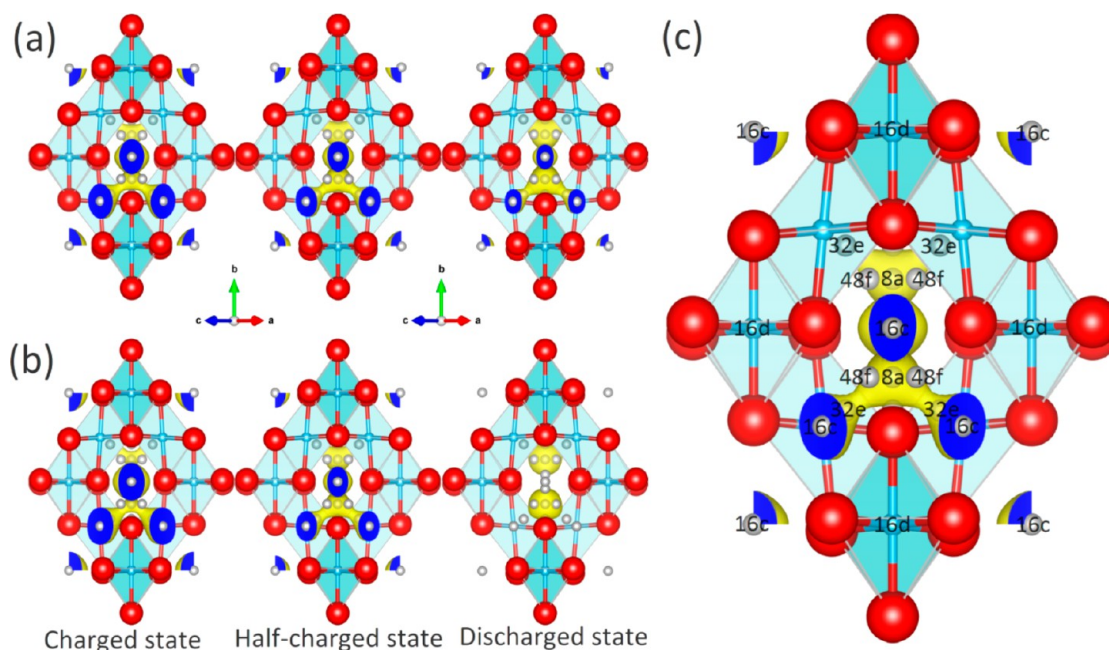


Figure 8. Fourier-difference maps showing only negative nuclear density (yellow) overlaid with the refined $\text{Li}_{4+z}\text{Ti}_5\text{O}_{12}$ structure for battery-1 (a) and battery-2 (b) at various battery SOC. For LTO-1, the NPD data were taken at 480–490, 605–615, and 740–750 min, representing the charged, half-charged, and discharged states, respectively. For LTO-2, these states corresponded to data at 705–715, 895–905, and 1135–1145 min, respectively. The maps show half of the view of the full unit cell shown in Figure 6, with the view along the c axis shown in Figure S10. O atoms are shown in red, Li is shown in gray with sites marked in the same manner as for the LTO-1 half-charged figure, and Ti and Li at the 16d site are shown in cyan (and marked). The contour levels (yellow) are adjusted to be the same for direct comparison. A larger image detailing the Li sites is also shown (c) using the result for LTO-1 at the half-charged state.

replenished during lithiation faster in LTO-2 than in LTO-1, which is based on the following arguments:

- (1) According to Vegard's law^{36,37} and our previous in situ NPD analysis of electrodes,²⁵ the nonmonotonic change in the $\text{Li}_{4+z}\text{Ti}_5\text{O}_{12}$ lattice reflects the variation of Li occupation at the 8a and 16c sites in $\text{Li}_{4+z}\text{Ti}_5\text{O}_{12}$. The similar variation between the LTO-1 and LTO-2 lattices as a function of the state-of-charge (Figure S2) indicates that the Li sites are populated similarly and that the lithiation–delithiation processes are similar.
- (2) The smaller particle size of LTO-2 results in a shorter mean free path for Li^+ diffusion, which, when combined with the slower rate of population of the 16c site in LTO-2 relative to LTO-1, results in the rate of transfer out of the 8a site being slower than the rate of its repopulation.

Together with the observed increase in the lattice parameter during initial lithiation (Figure 4), the presence of Li at the 8a site and the absence of Li at the 16c site in both anodes may suggest alternative pathways for the inward diffusion of Li^+ , although the determination of such pathways is difficult using the in situ NPD data. Laumann et al.³⁸ suggest that Li diffusion between the 8a and 16c sites occurs via the 32e site, and Wilkening et al. suggest that a 48f site may be involved in the migration of Li within $\text{Li}_4\text{Ti}_5\text{O}_{12}$.³⁹ To consider these possibilities, we examined the Fourier-difference nuclear density maps using the refined $\text{Li}_{4+z}\text{Ti}_5\text{O}_{12}$ phases with the Li at the 8a and 16c sites removed and the NPD data measured at the charged, half-charged, and discharged states and summed over two data sets (a total of 10 min at each SOC) (Figure 8).

The Fourier-difference maps overlaid with the $\text{Li}_{4+z}\text{Ti}_5\text{O}_{12}$ structures with Li at the 8a and 16c sites removed at the three SOC reveal no significant difference between the path for Li

diffusion in LTO-1 and LTO-2. The results shown in Figure 8 do not support Li at the 48f site, with the view along the c axis in Figure S10 clearly showing an absence of residual nuclear density surrounding this site. However, a small amount of residual negative nuclear density surrounds the 32e site, indicating the possibility that this site is involved in the Li-diffusion path, perhaps acting as a bridge connecting the 8a and 16c sites and lowering the energy barrier for diffusion, as suggested by Laumann et al.³⁸ The depth of density in Figure 8 represents the relative abundance of Li at each site, with the exception of the 16d site, which is also occupied by Ti, where Ti also has a negative neutron-scattering length. The evolution of the density distribution on going from the charged to discharged states (during delithiation) reveals that for both anodes the Li concentration at 8a sites increases, whereas the Li concentration at the 16c site decreases, showing good agreement with the calculated site occupation of Li at 8a and 16c (Figure 7). We note that the relative concentration of Li at the 8a and 16c sites differs significantly between LTO-1 and LTO-2, corroborating our result of dissimilarities in the lattice parameter evolution of LTO-1 and LTO-2. For example, at the half-charged state, it can be seen that although both anodes have similar nuclear-density shapes the site with most intense negative density differs for LTO-1 and LTO-2, where the strongest negative density is found at the 8a site in LTO-1 and at the 16c site for LTO-2. Overall, the maps again agree well with the evolution of the Li 8a and 16c site occupation shown in Figure 7.

During battery charge, the anode is reduced and the Ti valence drops from 4^+ to 3.4^+ when forming $\text{Li}_7\text{Ti}_5\text{O}_{12}$ and to 3^+ when forming the Li-excess $\text{Li}_9\text{Ti}_5\text{O}_{12}$. The coulombic attraction between Ti and O increases with Ti valence, as reflected by Ti–O bond length changes. Using the approach

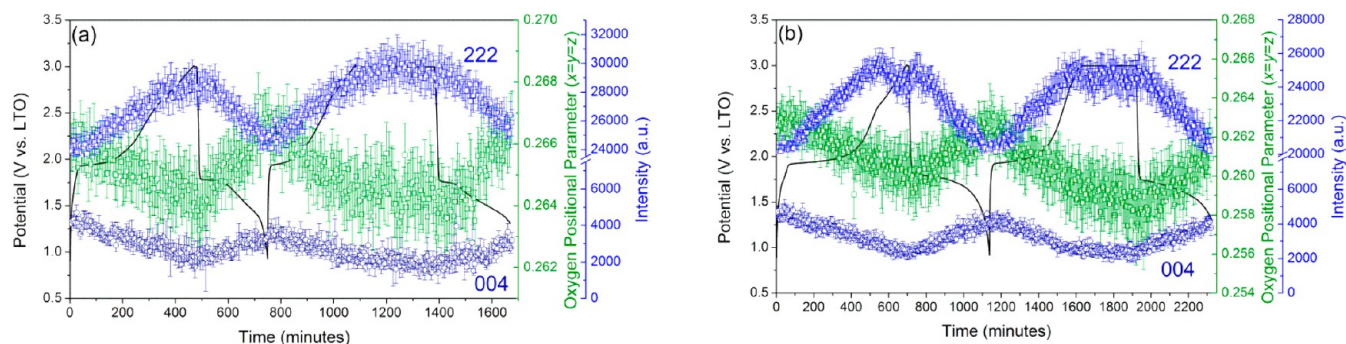


Figure 9. O positional parameter and $\text{Li}_{4+z}\text{Ti}_5\text{O}_{12}$ 222 and 004 reflection intensity in LTO-1 (a) and LTO-2 (b) during battery charge and discharge. Battery voltage is also shown.

taken in our previous work,²¹ we correlate the change in the O positional parameter to the Ti oxidation state and this, in turn, to the $\text{Li}_4\text{Ti}_5\text{O}_{12}$ 222 and 004 reflection intensities.

To track the O positional parameter effectively, it was necessary to fix the Li occupancy at the 8a and 16c sites in the sequential Rietveld refinement. The variation of the O positional parameter in LTO-1 and LTO-2 during battery cycling is shown in Figure 9. It can be seen that the O atom moves further from the Ti atom as the average Ti valence decreases during charge and that this change is associated with changes in the measured $\text{Li}_{4+z}\text{Ti}_5\text{O}_{12}$ 222 and 004 reflection intensities. The O positional parameter and $\text{Li}_{4+z}\text{Ti}_5\text{O}_{12}$ 222 reflection intensity changes during charge/discharge help to complete the picture of the $\text{Li}_4\text{Ti}_5\text{O}_{12}$ structural changes in the $\text{LiFePO}_4\|\text{Li}_4\text{Ti}_5\text{O}_{12}$ cell. By combining the evolution of $\text{Li}_{4+z}\text{Ti}_5\text{O}_{12}$ lattice and the O positional parameters with battery cycling, we can calculate the Ti–O bond length. We estimate the valence of Ti at the 16d site during the battery charge and discharge using the bond-valence sum (BVS) method,⁴⁰ noting that the method will yield an approximate Ti valence because Ti shares the 16d site with Li. The ideal $\text{Ti}^{4+}\text{--O}^{2-}$ bond length of 1.815 Å and empirical constant of 0.37 Å⁴⁰ were used in this estimation. The BVS of Ti in $\text{Li}_{4+z}\text{Ti}_5\text{O}_{12}$ during battery charge–discharge is shown in Figure 10, which reveals a decrease in Ti valence during lithiation (reduction during charge) and an increase during delithiation (oxidation during discharge), as expected.

CONCLUSIONS

Neutron-friendly $\text{LiFePO}_4\|\text{Li}_4\text{Ti}_5\text{O}_{12}$ cells were used in an in situ neutron powder diffraction study of two $\text{Li}_4\text{Ti}_5\text{O}_{12}$ anodes with differing particle sizes during charge–discharge battery cycling. By modeling the near-zero-strain $\text{Li}_4\text{Ti}_5\text{O}_{12}$ material as a solid-solution reaction, we revealed the underlying mechanism for particle-size-induced changes in battery performance. The variation in the lattice parameter, site-dependent Li concentration, and oxidation state of Ti (the redox-active transition metal) in the anodes was monitored, and all of these point to an increase in the number of Li ions migrating as a result of the reduced path length in the smaller-particle-sized anode rather than a change in the Li-migration pathway. The lattice of both anodes during continuous lithiation undergoes expansion followed by a gradual contraction before expanding again. We reconciled the measured lattice parameter changes with our measurement of Li at specific sites within the $\text{Li}_4\text{Ti}_5\text{O}_{12}$ crystal structure and found that Li migrates from the 8a to the 16c site in both anodes. Despite the similar trends of $\text{Li}_4\text{Ti}_5\text{O}_{12}$ lattice evolution and Li location during battery

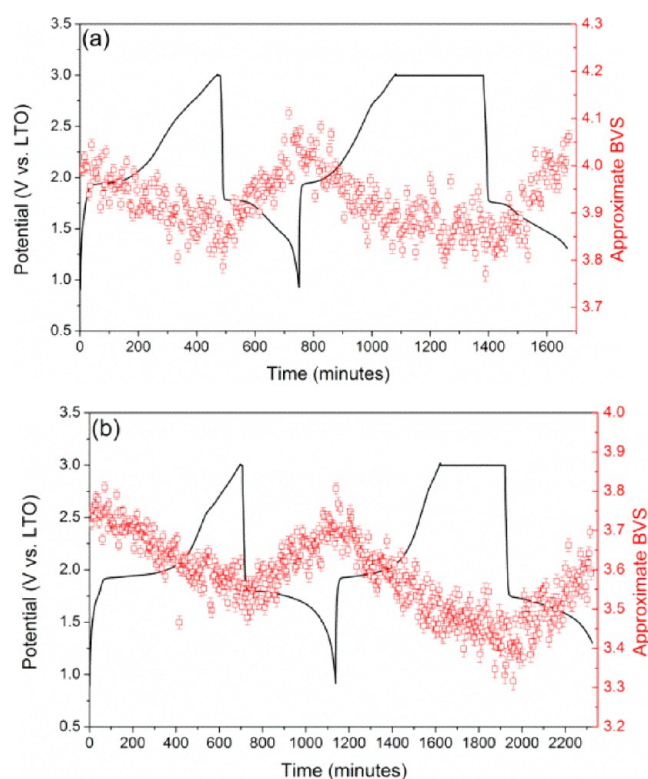


Figure 10. Approximate BVS for Ti in LTO-1 (a) and LTO-2 (b) during battery charge and discharge. Voltage is also shown.

cycling, we note that the smaller-particle-sized anode undergoes a much faster rate of change, 20.7(3)% during lithiation and 5.5(14)% during delithiation, than its larger-particle-sized counterpart, consistent with the larger measured capacity.

Our analysis of Fourier-difference nuclear density maps also indicates that the 32e site is involved in the Li diffusion in both anodes, but it does not evidence participation of a 48f site in this process.

Neutron powder diffraction was again shown to be an excellent tool for the study of electrode materials for Li-ion batteries, particularly when used to probe the real-time crystallographic changes of the materials in an operating battery during charge–discharge cycling.

ASSOCIATED CONTENT

Supporting Information

Crystallographic details of the as-prepared samples and of the $\text{Li}_{4+z}\text{Ti}_5\text{O}_{12}$ used in the in situ analysis; figures-of-merit for

sequential refinements; rate of change of LTO 222 and 004 reflection intensity; Rietveld profile fit and SEM micrograph for the LiFePO_4 ; sequential NPD patterns of battery-1 and battery-2 during cycling; in situ NPD single-peak fitting results and electrochemical behavior of the LiFePO_4 cathode in battery-1 and battery-2; Rietveld profiles for the as-prepared battery-1 and battery-2 samples; charge–discharge curves and the calculated capacities for battery-1 and battery-2 during the NPD experiment; linear fits of the lattice parameter of LTO-1 and LTO-2 as a function of state-of-charge; results from linear fits to the charge–discharge evolution of Li content in LTO-1 and LTO-2; and the Fourier-difference nuclear density maps overlaid with the LTO-1 and LTO-2 structures shown along the c axis (PDF). This material is available free of charge via the Internet at <http://pubs.acs.org>.

AUTHOR INFORMATION

Corresponding Authors

*(V.K.P.) E-mail: vanessa.peterson@ansto.gov.au; Tel.: +61 9717 9401.

*(S.-h.W.) E-mail: shwu@ttu.edu.tw; Tel.: +886-2-25922458; Fax: +886-2-25936897.

Author Contributions

The manuscript was written through contributions of all authors. All authors have given approval to the final version of the manuscript.

Notes

The authors declare no competing financial interest.

ACKNOWLEDGMENTS

We acknowledge the travel support funded by the National Synchrotron Radiation Research Center (2013-3-100-1). We are also grateful to Professor Lin, Jeng-Yu of Tatung University for providing the $\text{Li}_4\text{Ti}_5\text{O}_{12}$ sample, Tatung Fine Chemicals Co., Taiwan for providing the LiFePO_4 sample, and the staff members at the Bragg Institute, ANSTO for their operations support.

ABBREVIATIONS

NPD, neutron powder diffraction; LIB, Li-ion battery; BVS, bond-valence summation; LAMP, large-array manipulation program; SOC, state-of-charge; PVDF, poly(vinylidene)-difluoride

REFERENCES

- (1) Nishi, Y. *J. Power Sources* **2001**, *100*, 101–106.
- (2) Ohzuku, T.; Ueda, A.; Yamamoto, N. *J. Electrochem. Soc.* **1995**, *142*, 1431–1435.
- (3) Scharner, S.; Weppner, W.; Schmid-Beurmann, P. *J. Electrochem. Soc.* **1999**, *146*, 857–861.
- (4) Panero, S.; Reale, P.; Ronci, F.; Scrosati, B.; Perfetti, P.; Rossi Albertini, V. *Phys. Chem. Chem. Phys.* **2001**, *3*, 845–847.
- (5) Cho, J.; Kim, Y. J.; Kim, T.-J.; Park, B. *Angew. Chem.* **2001**, *113*, 3471–3473.
- (6) Ronci, F.; Reale, P.; Scrosati, B.; Panero, S.; Rossi Albertini, V.; Perfetti, P.; di Michiel, M.; Merino, J. M. *J. Phys. Chem. B* **2002**, *106*, 3082–3086.
- (7) Wang, C.; Appleby, A. J.; Little, F. E. *Electrochim. Acta* **2001**, *46*, 1793–1813.
- (8) Shu, J. *Electrochem. Solid-State Lett.* **2008**, *11*, A238–A240.
- (9) He, Y.-B.; Tang, Z.-Y.; Song, Q.-S.; Xie, H.; Liu, Y.-G.; Xu, Q. *J. Electrochem. Soc.* **2008**, *155*, A481–A487.
- (10) Shen, L.; Zhang, X.; Uchaker, E.; Yuan, C.; Cao, G. *Adv. Energy Mater.* **2012**, *2*, 691–698.
- (11) Bruce, P. G.; Scrosati, B.; Tarascon, J.-M. *Angew. Chem.* **2008**, *47*, 2930–2946.
- (12) Wagemaker, M.; Simon, D. R.; Kelder, E. M.; Schoonman, J.; Ringpfeil, C.; Haake, U.; Lützenkirchen-Hecht, D.; Frahm, R.; Mulder, F. M. *Adv. Mater.* **2006**, *18*, 3169–3173.
- (13) Striebel, K.; Shim, J.; Srinivasan, V.; Newman, J. J. *Electrochem. Soc.* **2005**, *152*, A664–A670.
- (14) Zhu, G.-N.; Wang, Y.-G.; Xia, Y.-Y. *Energy Environ. Sci.* **2012**, *5*, 6652–6667.
- (15) Jiang, C.; Hosono, E.; Ichihara, M.; Honma, I.; Zhou, H. *J. Electrochem. Soc.* **2008**, *155*, A553–A556.
- (16) Guo, X.; Wang, C.; Chen, M.; Wang, J.; Zheng, J. *J. Power Sources* **2012**, *214*, 107–112.
- (17) Cho, W.; Song, J. H.; Park, M.-S.; Kim, J.-H.; Kim, J.-S.; Kim, Y.-J. *J. Electrochem. Sci. Technol.* **2010**, *1*, 85–91.
- (18) Borghols, W. J. H.; Wagemaker, M.; Lafont, U.; Kelder, E. M.; Mulder, F. M. *J. Am. Chem. Soc.* **2009**, *131*, 17786–17792.
- (19) Cai, L.; An, K.; Feng, Z.; Liang, C.; Harris, S. J. *J. Power Sources* **2013**, *236*, 163–168.
- (20) Du, G.; Sharma, N.; Peterson, V. K.; Kimpton, J. A.; Jia, D.; Guo, Z. *Adv. Funct. Mater.* **2011**, *21*, 3990–3997.
- (21) Pang, W. K.; Sharma, N.; Peterson, V. K.; Shiu, J.-J.; Wu, S.-h. *J. Power Sources* **2014**, *246*, 464–472.
- (22) Sharma, N.; Du, G.; Studer, A. J.; Guo, Z.; Peterson, V. K. *Solid State Ionics* **2011**, *199–200*, 37–43.
- (23) Sharma, N.; Peterson, V. K. *Electrochim. Acta* **2013**, *101*, 79–85.
- (24) Sharma, N.; Reddy, M. V.; Du, G.; Adams, S.; Chowdari, B. V. R.; Guo, Z.; Peterson, V. K. *J. Phys. Chem. C* **2011**, *115*, 21473–21480.
- (25) Sharma, N.; Yu, D.; Zhu, Y.; Wu, Y.; Peterson, V. K. *Chem. Mater.* **2013**, *25*, 754–760.
- (26) Colin, J.-F.; Godbole, V.; Novák, P. *Electrochem. Commun.* **2010**, *12*, 804–807.
- (27) Padhi, A. K.; Nanjundaswamy, K. S.; Goodenough, J. B. *J. Electrochem. Soc.* **1997**, *144*, 1188–1194.
- (28) Padhi, A. K.; Nanjundaswamy, K. S.; Masquelier, C.; Okada, S.; Goodenough, J. B. *J. Electrochem. Soc.* **1997**, *144*, 1609–1613.
- (29) Liss, K.-D.; Hunter, B.; Hagen, M.; Noakes, T.; Kennedy, S. *Physica B* **2006**, *385–386*, 1010–1012.
- (30) Hunter, B. *Rietica – A Visual Rietveld Program*; International Union of Crystallography Commission on Powder Diffraction Newsletter No. 20: 1998; <http://www.rietica.org>.
- (31) Studer, A. J.; Hagen, M. E.; Noakes, T. J. *Phys. B* **2006**, *385–386*, 1013–1015.
- (32) Rodriguez-Carvajal, J. *Phys. B* **1993**, *192*, 55–69.
- (33) Roisnel, T.; Rodriguez-Carvajal, J. In *WinPLOTR: A Windows Tool for Powder Diffraction Patterns Analysis*; Materials Science Forum, Proceedings of the Seventh European Powder Diffraction Conference (EPDIC 7), Barcelona, Spain, May 20–23, 2000; Delhez, R., Mittenmeijer, E. J., Eds.; Trans Tech Publications: Switzerland, 2001; pp 118–123.
- (34) Richard, D.; Ferrand, M.; Kearley, G. J. *J. Neutron Res.* **1996**, *4*, 33–39.
- (35) Palomares, V.; Goni, A.; Iturrondobea, A.; Lezama, L.; de Meaza, I.; Bengoechea, M.; Rojo, T. *J. Mater. Chem.* **2012**, *22*, 4735–4743.
- (36) Denton, A. R.; Ashcroft, N. W. *Phys. Rev. A* **1991**, *43*, 3161–3164.
- (37) Vegard, L. *Z. Phys.* **1921**, *5*, 17–26.
- (38) Laumann, A.; Boysen, H.; Bremholm, M.; Fehr, K. T.; Hoelzel, M.; Holzapfel, M. *Chem. Mater.* **2011**, *23*, 2753–2759.
- (39) Wilkening, M.; Amade, R.; Iwaniak, W.; Heitjans, P. *Phys. Chem. Chem. Phys.* **2007**, *9*, 1239–1246.
- (40) Brown, I. D.; Altermatt, D. *Acta Crystallogr., Sect. B* **1985**, *41*, 244–247.